ACSNANO

www.acsnano.org

ARTICLE

Red Emission from Copper-Vacancy Color Centers in Zinc Sulfide Colloidal Nanocrystals

Sarah M. Thompson, Cüneyt Şahin, Shengsong Yang, Michael E. Flatté, Christopher B. Murray, Lee C. Bassett,* and Cherie R. Kagan*

Cite This: *ACS Nano* 2023, 17, 5963−5973

Read Online

ACCESS | Metrics & More | Article Recommendations | Supporting Information

ABSTRACT: Copper-doped zinc sulfide (ZnS:Cu) exhibits down-conversion luminescence in the UV, visible, and IR regions of the electromagnetic spectrum; the visible red, green, and blue emission is referred to as R-Cu, G-Cu, and B-Cu, respectively. The sub-bandgap emission arises from optical transitions between localized electronic states created by point defects, making ZnS:Cu a prolific phosphor material and an intriguing candidate material for quantum information science, where point defects excel as single-photon sources and spin qubits. Colloidal nanocrystals (NCs) of ZnS:Cu are particularly interesting as hosts for the creation, isolation, and measurement of quantum defects, since their size, composition, and surface chemistry can be precisely tailored for biosensing and optoelectronic applications. Here, we present a method for synthesizing colloidal ZnS:Cu NCs that emit primarily R-Cu, which has been proposed to arise from the Cu_{Zn}-V_S complex, an impurity-vacancy point defect structure analogous to well-known quantum defects in other materials that produce favorable optical and spin dynamics. First-principles calculations confirm the thermodynamic stability and electronic structure of Cu_{Zn}-V_S. Temperature- and time-dependent optical properties of ZnS:Cu NCs show blueshifting luminescence and an anomalous plateau in the intensity dependence as temperature is increased from 19 K to 290 K, for which we propose an empirical dynamical model based on thermally activated coupling between two manifolds of states inside the ZnS bandgap. Understanding of R-Cu emission dynamics, combined with a controlled synthesis method for obtaining R-Cu centers in colloidal NC hosts, will greatly facilitate the development of Cu_{Zn}-V_S and related complexes as quantum point defects in ZnS.

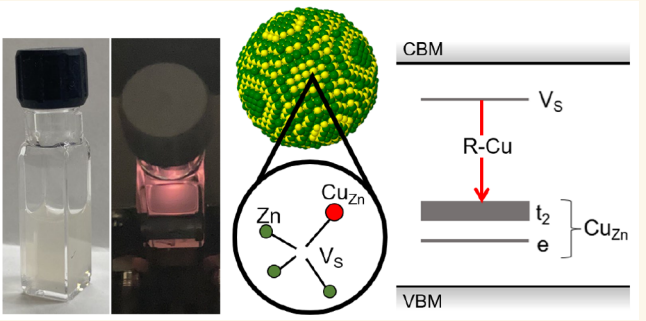

KEYWORDS: *nanocrystals, zinc sulfide, color center, impurity doping, transition metals, photoluminescence*

Controlled impurity doping of wide-bandgap semiconductors can be used to introduce color centers, which are point defects that activate sub-bandgap, optical photoluminescence (PL). Color centers can serve as sources of tunable PL for bioimaging and optoelectronic applications,[1,2] as well as localized, optically addressable, electronic spin states for applications in quantum information science.[3,4] For all of these applications, colloidal nanocrystals (NCs) can provide advantages over analogous, bulk materials because they can be processed using wet-chemical methods, and their large surface areas and effects of quantum confinement allow for highly tunable optical and electronic properties.[5] While the focus of PL studies in impurity-doped NCs is frequently on emission mechanisms that involve the host bandgap and confinement effects, control of deeply sub-bandgap PL emission associated with localized defect states is important for developing suitable color centers in materials for QIS applications. Impurity-doped ZnS has long been exploited as a UV, visible, and NIR luminescent material in its bulk and colloidal NC forms, and it has more recently been studied as a potential host material for defect-based quantum emitters and quantum bits, or defect qubits.[6,7] Cu-doping of ZnS introduces sub-bandgap red, green, and blue PL emission bands that are associated with color centers known respectively as R-Cu, G-Cu, and B-Cu. R-Cu color centers are particularly interesting thanks to their peak PL emission in the NIR biological window. However, R-Cu remains under-utilized since it is rarely observed in colloidal ZnS:Cu NCs, which typically emit visible PL dominated by B-Cu and G-Cu.[8−10]

Received: January 6, 2023
Accepted: March 7, 2023
Published: March 9, 2023

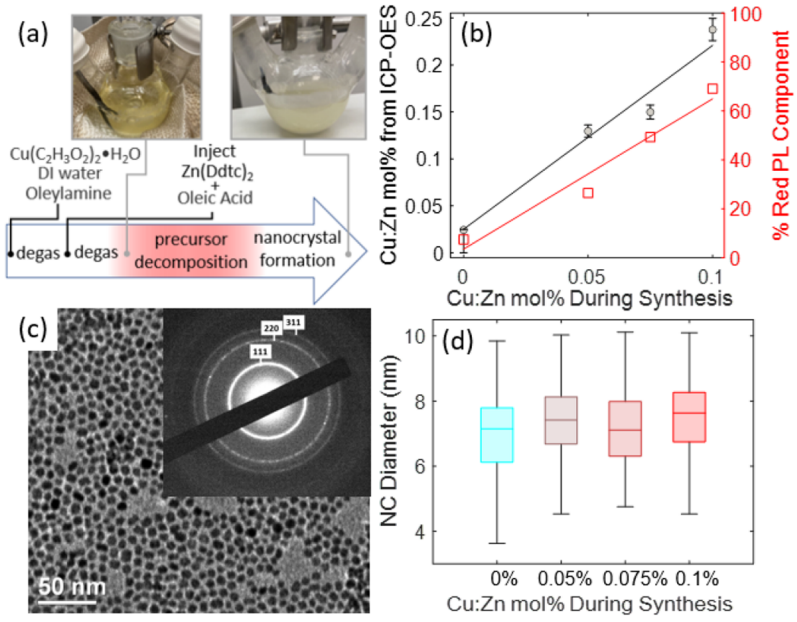

Figure 1. ZnS:Cu NC synthesis and structure. (a) Schematic of the synthesis of R-Cu-emitting ZnS:Cu NCs, where red represents the application of heat. Photographs show the reaction vessel before and after NC formation. (b) Cu:Zn mol % measured by ICP-OES (black circles) as a function of the Cu:Zn mol % added to the synthesis pot. The component weight of the R-Cu peak when the total PL spectrum is decomposed by non-negative matrix factorization (red squares and right-hand vertical axis) also scales with the Cu:Zn mol %. The R^2 values for the linear regression fits (black and red lines) are 0.917 and 0.957, respectively. (c) TEM image and electron diffraction pattern of a sample of ZnS:Cu NCs with 0.1 mol % Cu:Zn. (d) Distribution of NC diameters for samples of 100 NCs measured from TEM images obtained for each Cu:Zn ratio (0−0.1 mol %).

Past studies have indicated that R-Cu emission in bulk ZnS:Cu arises from a defect complex consisting of a substitutional copper impurity (Cu_{Zn}) and a sulfur vacancy (V_S) in a nearest-neighbor Cu_{Zn}-V_S complex.[11] Compared to transition metal-doped phosphors like ZnS:Mn that rely on electric-dipole-forbidden, intra-d-shell transitions between substitutional Mn_{Zn} levels to produce visible PL, the mixed orbital character and lowered symmetry of the Cu_{Zn}-V_S complex are associated with more dipole-allowed radiative transitions,[12] and therefore shorter optical lifetimes, as desired for many applications. Moreover, the symmetry of the Cu_{Zn}-V_S complex is described by the C_{3v} point group, which is characteristic of well-developed defect qubits[13,14] and is a key factor in producing favorable defect orbital and spin structures.[4] R-Cu emission has further been associated with electron paramagnetic resonance (EPR) spectra, which indicate a paramagnetic ground state.[15] These characteristics are especially compelling in combination with the favorable properties of ZnS as a host for defect qubits, which include a high natural abundance of spin-free nuclei and relatively weak spin−orbit coupling, as well as the ease of ZnS colloidal NC synthesis and surface modification compared to host materials such as diamond.[5,16]

Here, we report the synthesis and characterization of colloidal ZnS:Cu NCs emitting visible PL dominated by R-Cu. We study the structural, compositional, and time- and temperature-dependent optical properties of NCs synthesized with 0, 0.05, 0.075, and 0.1 mol % Cu:Zn. The R-Cu emission intensity scales with the copper concentration, and the R-Cu emission band exhibits complex temperature- and time-dependent properties. In particular, the R-Cu emission peak blueshifts with increasing temperature from 19 K to 290 K, consistent with observations in bulk ZnS:Cu,[11] and the R-Cu emission intensity as a function of temperature shows an anomalous plateau between 150 and 270 K. We propose a single mechanism to explain the temperature-dependent peak energy, intensity, and lifetime based on thermally activated carrier transfer between two manifolds of radiative states. This mechanism is consistent with time-resolved PL measurements showing the presence of two distinct radiative transitions in the R-Cu band at low temperature. Drawing from first-principles calculations, we discuss the role of defect species, spatial arrangement, and charge state in producing the manifolds of states responsible for measured R-Cu characteristics. A detailed understanding of these characteristics can facilitate the realization of protocols for initialization, readout, and control of the defect's charge and spin states for development of a quantum defect architecture.

RESULTS AND DISCUSSION

Synthesis of ZnS:Cu NCs with R-Cu Emission. ZnS NCs are synthesized using the single-source precursor approach developed by Zhang et al.,[17] in which zinc diethyldithiocarbamate ($Zn(Ddtc)_2$) is thermally decomposed in oleic acid (OA) and oleylamine (OM); see Figure 1a. In previously reported syntheses of colloidal ZnS:Cu NCs, the absence of R-Cu emission may result from unintentional Cl impurities introduced by $CuCl_2$ precursors, which are known to quench R-Cu in bulk ZnS:Cu along with Al, In, and Ga impurities.[11,15,18] To avoid the introduction of Cl impurities, we instead add a fixed volume (0.1 mL) of $Cu(CH_3COO)_2 \cdot H_2O$ dissolved in ultrapure DI water, with concentrations corresponding to Cu:Zn molar ratios of 0%, 0.05%, 0.075%, and 0.1%, to the synthesis pot prior to degassing. In the case of undoped ZnS NCs, the 0.1 mL addition consists of DI water only. Inductively coupled plasma−optical emission spectros-

https://doi.org/10.1021/acsnano.3c00191
ACS Nano 2023, 17, 5963−5973

copy (ICP-OES) and PL measurement results (Figure 1b) show that varying the concentration of the Cu precursor directly influences the final Cu concentration in the NC samples, as well as the relative intensity of the red PL emitted by the NCs. The PL measurement results are discussed further in the next subsection.

A representative TEM image of ZnS:Cu NCs with 0.1 mol % Cu:Zn (Figure 1c) shows that the samples are composed of 7.2 ± 1.2 nm diameter particles. The NC size distribution remains consistent across differently doped samples (Figure 1d). Electron diffraction measurements (inset, Figure 1c) exhibit peaks at 2Θ values that correspond to the ⟨111⟩, ⟨220⟩, and ⟨311⟩ planes of sphalerite (zinc blende), according to PDF# 98-000-04053.

Room-Temperature Optical Characterization. PL emission spectra from NC samples containing the four different Cu concentrations are shown in Figure 2a. The intrinsic, background PL peak with emission wavelength, λ_{em}, between 430 and 600 nm, is present regardless of Cu concentration. This PL feature is characteristic of undoped ZnS NCs and is widely accepted to arise from radiative transitions between intrinsic defect states inside the ZnS bandgap created by Zn and S vacancies (V_{Zn} and V_S) and interstitials (Zn_i and S_i).[19−21] Similar PL is also observed from bulk, undoped ZnS, with features being attributed to both intrinsic defects and unintentional impurities.[22]

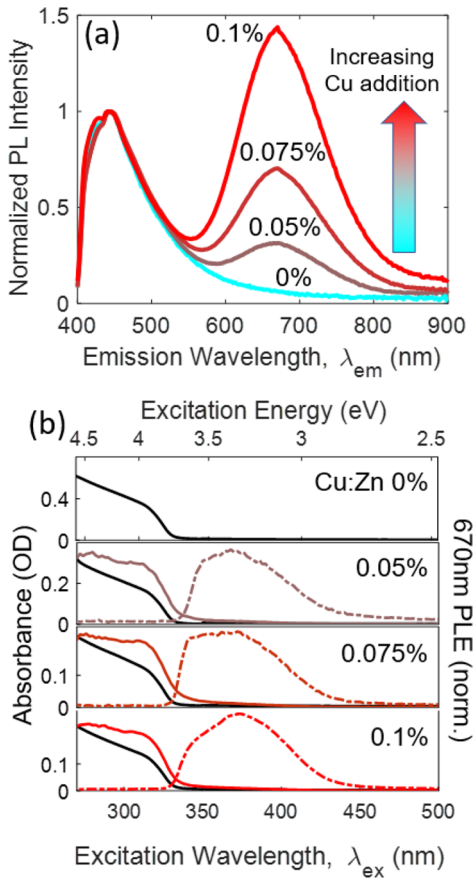

Figure 2. Room-temperature optical properties. (a) PL spectra under continuous-wave excitation at λ_{ex} = 375 nm, normalized to the PL intensity at λ_{em} = 442 nm from ZnS NCs synthesized with 0−0.1 mol % Cu:Zn. (b) Absorption spectra (black curves) and corresponding λ_{em} = 670 nm PLE spectra for dilute (<0.5 mg/mL) NC dispersions (solid colored curves). Dashed colored curves indicate PLE spectra for concentrated (10 mg/mL) NC dispersions with above-bandgap absorbance greater than OD = 4.0. PLE spectra monitor the emission intensity at λ_{em} = 670 nm as a function of λ_{ex} and are normalized to their peak wavelength values.

Distinct emission with λ_{em} centered at 670 nm is observed in the Cu-doped NCs with a relative intensity that increases with the Cu:Zn molar ratio. The PL spectra of Figure 2a are decomposed using nonnegative matrix factorization (SI Section 1) in order to calculate the relative strengths of the intrinsic and dopant-induced components, yielding the concentration dependence plotted in Figure 1b. Absorption spectra and λ_{em} = 670 nm PLE spectra for all NC materials are shown in Figure 2b. From the absorption spectra, we construct Tauc plots (SI Section 2) and extract bandgap energies between 3.77 and 3.79 eV.

The λ_{em} = 670 nm PL and PLE spectra in Figure 2 align well with those reported for R-Cu in bulk ZnS:Cu, which also peaks at λ_{em} = 670 nm at room temperature and is attributed to transitions between V_S levels and Cu_{Zn} levels inside the ZnS bandgap.[18] The PLE spectra of Figure 2b show that the λ_{em} = 670 nm PL in all doped NC samples is excited by the ZnS host, more easily observable in measurements of dilute NC dispersions (<0.5 mg/mL, solid curves in Figure 2b), as well as by sub-bandgap wavelengths in the range λ_{ex} = 330−450 nm, more readily seen in concentrated (10 mg/mL, dashed curves) NC dispersions. The sub-bandgap excitation allows excitation of a greater number of color centers in concentrated samples because it is more efficiently transmitted throughout the sample volume (SI Section 3). Thus, the PLE from concentrated NC dispersions more closely resembles PLE for defect emission from ZnS bulk crystals and powders.[9,11,22] We use sub-bandgap, 375 nm excitation in this work to achieve overall higher PL count rates and allow efficient measurement of temperature-dependent PL from deposited films of ZnS:Cu NCs. The polarization dependence of the sub-bandgap PLE in bulk ZnS:Cu indicates a nearest-neighbor configuration of V_S and Cu_{Zn} with C_{3v} point-group symmetry,[11] consistent with more recent extended X-ray absorption fine structure (EXAFS) measurements in ZnS:Cu NCs.[23] R-Cu is quenched when bulk ZnS:Cu phosphors are fired in atmospheres containing high sulfur pressure,[11] further supporting the role of V_S levels in the PL.

Compared to their bulk counterparts, impurity doping of NC materials can be challenging to achieve and to confirm.[24] The alignment between the R-Cu PL/PLE spectra we measure here and that arising from bulk ZnS:Cu are suggestive of successful Cu doping of the ZnS:Cu NCs, since there is extensive evidence that R-Cu in bulk ZnS:Cu is activated by Cu substitutionally occupying Zn sites. We additionally carry out studies in which we deposit NC thin films and treat them with methanol and methanolic Na_2S and $Zn(CO_2CH_3)_2{\cdot}2H_2O$ solutions known to remove organic ligands and to strip surface cations[25] and to enrich the NC surface in S^{2-} or Zn^{2+}, respectively,[26,27] altering the presence or environment of Cu cations if they are on the surface. In all cases, the surface treatments do not quench or enhance the R-Cu PL from our NCs, again consistent with successful Cu doping of their cores (SI Section 4).

Variable-Temperature Studies Probing the Origins of Cu-Induced Sub-Bandgap PL/PLE. NCs are drop-cast onto sapphire substrates and loaded inside an evacuated cryostat for

https://doi.org/10.1021/acsnano.3c00191
ACS Nano 2023, 17, 5963−5973

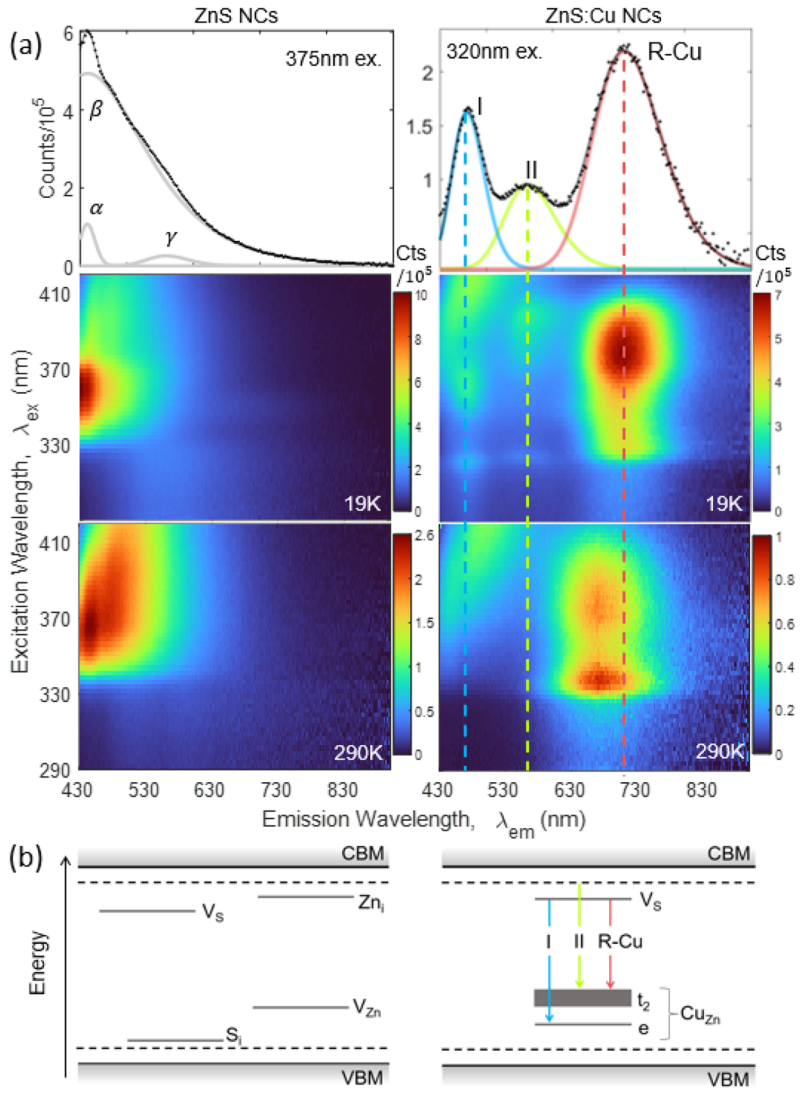

Figure 3. Temperature-dependent PL/PLE. (a) PL spectra (top) and PL/PLE maps (below) of films of ZnS NCs synthesized with 0 mol % (left) and 0.1 mol % Cu:Zn (right), measured at 19 K and room temperature. The PL spectra extracted from the 19 K PL/PLE maps are photoexcited at λ_{ex} = 375 nm and λ_{ex} = 320 nm for the ZnS NC and ZnS:Cu NC films, respectively, to show the clearest peak separation and spectrally reduce intrinsic PL in the case of ZnS:Cu NCs. (b) Energy level diagrams showing key defect states responsible for sub-bandgap PL emission in the undoped and doped NCs. Dashed lines represent shallow surface defect states. Arrows are used to indicate assigned radiative transitions in the doped NCs, which involve different sublevels of the Cu_{Zn} 3d shell. The t_2 level is indicated with a heavier line to suggest that it may be further split into e and a sublevels depending on the Cu_{Zn} impurity site coordination.

temperature- and time-dependent spectroscopic measurements. Figure 3 shows PL/PLE maps of ZnS NCs without Cu doping (Cu:Zn at 0 mol %) and with Cu doping (Cu:Zn 0.1 mol %), measured at 19 K and at 290 K. The NC films are highly absorbing, and therefore the above-bandgap PLE is relatively diminished, as discussed in the previous section, consistent with the dashed PLE curves in Figure 2b. PL from the undoped ZnS NCs is dominated by intrinsic PL at all temperatures. The 19 K PL spectrum from the undoped ZnS NCs (λ_{ex} = 375 nm) can be described using three Gaussian peaks, which are labeled α, β, and γ in Figure 3a. Peaks α and β dominate the PL for λ_{ex} > 330 nm (corresponding to sub-bandgap excitation of the ZnS NCs), and their peak emission wavelength varies with λ_{ex}. The third peak observable in the undoped film, peak γ, remains relatively fixed regardless of λ_{ex} and is the only peak observed in this spectral region for λ_{ex} < 330 nm.

For ZnS:Cu NCs, the 19 K PL spectrum (λ_{ex} = 320 nm) shows R-Cu emission, as well as blue and green emission peaks labeled I and II (Figure 3). The three PL peaks are observed for λ_{ex} ranging from 290 to 420 nm. For λ_{ex} < 330 nm, to the blue of the ZnS bandgap wavelength, the sub-bandgap intrinsic PL is significantly diminished in intensity compared to peaks I, II, and R-Cu. The R-Cu peak is distinguishable at all temperatures, and the peak emission wavelength blueshifts from 709 nm at 19 K to 670 nm at room temperature. This observation is similar to the reported blueshift in bulk ZnS:Cu from 700 nm at 4 K to 670 nm at room temperature.[11,18] Peaks I and II, with λ_{em} = 471 nm and λ_{em} = 562 nm, respectively, are quenched at room temperature. The λ_{em} and fwhm values for PL labeled in Figure 3 are listed in Table 1. Line plots of the spectral data in the PL/PLE maps of Figure 3a are included in SI Section 5.

https://doi.org/10.1021/acsnano.3c00191
ACS Nano 2023, 17, 5963−5973

Table 1. Peak Positions and Widths for I, II, R-Cu, and α, β, and γ, from Gaussian Fitting of PL Data Shown in Figure 3

Cu:Zn mol %	label	λ_{em} (nm)	E_{em} (eV)	fwhm (eV)
0.1	I	471	2.61	0.13
0.1	II	562	2.19	0.21
0.1	R-Cu	709	1.74	0.27
0	α	440	2.81	0.17
0	β	442	2.65	1.12
0	γ	560	2.20	0.30

Figure 3b shows energy level diagrams containing key defect levels believed to activate PL in the undoped and doped NCs. In undoped ZnS, intrinsic PL is assigned to transitions between Zn_i, V_S, V_{Zn}, and S_i levels, for which the relative energy levels shown are agreed upon, but the exact energies are not known.[19,28] PL peaks activated by Cu doping the ZnS NCs, which can be spectrally separated from intrinsic PL as discussed in this section, are assigned to radiative transitions in the diagram. R-Cu emission arises from transitions between states primarily associated with V_S and the Cu_{Zn} t_2 levels.[18] We assign peak I to a transition between V_S levels and the lower-lying Cu_{Zn} e levels.[9] This assignment is supported by our measurement of a 0.87 eV energy difference between peak I and R-Cu PL, similar to the reported 0.86 eV energy difference between Cu_{Zn} t_2 and e levels.[29] Peak II is assigned to transitions between donor levels that are shallower than V_S, attributed here to surface defects, and the Cu_{Zn} t_2 levels.[30] We note that the state labels and identifications in Figure 3b are based on an approximate picture of isolated V_S and Cu_{Zn} in cubic ZnS, whereas the Cu_{Zn}-V_S is characterized by lowered C_{3v} symmetry and hybridization between these levels. We discuss this point in more detail later in the next section, drawing insight from theoretical calculations.

Figure 4a shows how time-resolved emission spectroscopy can be used to isolate R-Cu PL from the intrinsic background PL, since most of the intrinsic PL occurs within 250 ns of excitation while the R-Cu PL is longer lived. The room-temperature PL decay of ZnS:Cu NCs, excited with a pulsed excitation source at λ_{ex}= 375 nm and monitored at λ_{em}= 670 nm, is triexponential with decay time constants (τ_i) of τ_1 = 1.85 μs, τ_2 = 8.72 μs, and τ_3 = 26.47 μs. With 95% confidence, we find that these τ_i are consistent among all three Cu-doped samples (SI Section 6). At 19 K, time-resolved emission spectroscopy separates peaks I and II as well as R-Cu from the intrinsic background PL. Figure 4b shows that time-gating the PL from the ZnS:Cu NC samples yields an almost identical spectral shape to that of calculating the difference between the normalized, CW PL spectra from the doped NCs and the undoped NCs. The CW spectra in Figure 4b are normalized such that the PL intensities collected at 430 nm (the shortest emission wavelength in the measurement) are the same, as PL at this wavelength is expected to arise predominantly from intrinsic defects. The observation that nearly identical spectra are obtained, either by time-gating the doped spectrum or by subtracting the undoped CW spectrum, strongly supports that peaks I and II arise from Cu doping, along with the R-Cu peak, and these peaks coexist with the intrinsic PL in doped samples for sub-bandgap excitation.

First-Principles Calculations. R-Cu PL has been proposed to arise from a nearest-neighbor (NN) complex of Cu_{Zn} and V_S defects, rather than more distant associations.[11] To confirm the thermodynamic stability of the NN Cu_{Zn}-V_S complex, we use density functional theory (DFT) to calculate the formation energies, defect levels, and projected density of states (PDOS) for ground-state configurations of the complex in several charge states, as well as for the next-nearest-neighbor (NNN) complex. The results of these calculations are shown in Figure 5. We find that the formation energy of the NN Cu_{Zn}-V_S complex is lower than that of the NNN complex. The formation energy calculations in Figure 5a indicate that the two stable charge states are either negative (−1) or positive (+1), depending on the Fermi level, with the neutral (0) configuration always lying higher in energy. This is in contrast to the calculation for NN Cu_{Zn}-V_S in an unrelaxed ZnS lattice, which significantly increases the formation energy of all charge states, but particularly the negative and neutral configurations.

Figure 5b shows the defect levels and their projections at k = 0 for each charge state of the NN complex. These calculations qualitatively agree with the relative arrangement of levels in Figure 3b, with orange lines indicating the positions of two, higher-energy states derived from Zn dangling bonds surrounding the V_S site, and green lines indicating 10, lower-energy states derived from the Cu_{Zn} d-shell. The total density of states for pure ZnS and for ZnS containing a neutral Cu_{Zn}-V_S complex are included in SI Section 7. In the negatively charged complex, all 12 states are occupied, and the V_S-derived states are strongly mixed with the Cu_{Zn}-derived states. In the neutral complex, the V_S-derived states are only partially filled and are no longer mixed with the Cu_{Zn}-derived states. In the positively charged complex, only the Cu_{Zn}-derived states are occupied and the V_S-derived states are no longer easily

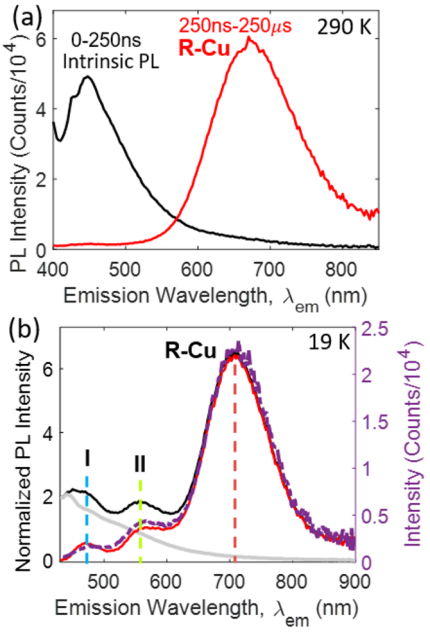

Figure 4. Isolation of Cu-activated PL. (a) Time-resolved emission spectra from ZnS:Cu NC films at 290 K under 375 nm, 1 kHz pulsed excitation, in which counts from the first 250 ns following the laser pulse (black) are plotted separately from subsequent counts (red), effectively separating the intrinsic background from the R-Cu peak emission. (b) PL spectra from ZnS:Cu NC (black trace) and undoped ZnS NC (gray trace) films, collected at 19 K with continuous wave, 375 nm excitation. Intensities are normalized at 430 nm. The difference spectrum (red curve) is almost identical to the time-gated spectrum from ZnS:Cu NC films under 375 nm, 500 kHz pulsed excitation (purple dashed curve).

https://doi.org/10.1021/acsnano.3c00191
ACS Nano 2023, 17, 5963−5973

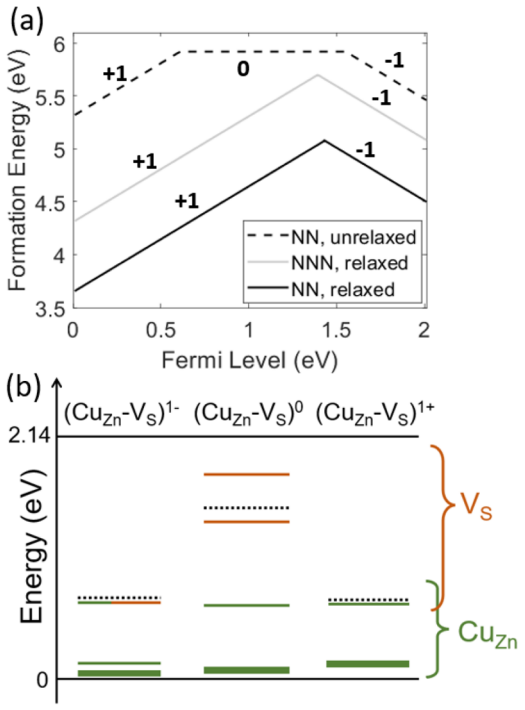

Figure 5. First-principles calculations. (a) Formation energies for nearest- and next-nearest-neighbor (NN and NNN, respectively) associations of Cu_{Zn} and V_S in ZnS, as a function of the Fermi level (solid curves). Charge states with respect to the ZnS lattice are indicated as −1, 0, and +1 for the negatively charged, neutral, and positively charged complex, respectively. The dashed curve shows the formation energy for the NN complex in an unrelaxed ZnS lattice. All formation energy calculations are performed under zinc-rich sulfur-poor thermodynamical stability conditions. (b) Defect levels at k = 0 for three different charge states of the NN Cu_{Zn}-V_S complex. Orange lines indicate V_S-derived states, and green lines indicate Cu_{Zn}-derived states. Solid lines indicate the valence band maximum (0 eV) and conduction band minimum (2.14 eV). Dotted lines indicate the Fermi level.

isolated, likely because they have been pushed far into the conduction band; however, this may be an artifact of well-known DFT bandgap errors (the estimated bandgap in this calculation is 2.14 eV, compared to the expected value around 3.6 eV), and the V_S states may still exist within the bandgap.

For the R-Cu transition depicted in Figure 3b to occur, there must be a hole in the higher-energy Cu_{Zn} states. This hole is likely created by photoionization of a Cu_{Zn} electron into the conduction band based on the large Stokes shift we observe between peak λ_{em} and peak λ_{ex} for R-Cu PL. It has also been proposed that this Stokes shift is a result of lattice relaxation around the excited complex when a Cu_{Zn} electron is transferred directly to a V_S state.[11,31] In this case, the excited V_S level lies above the conduction band minimum immediately after excitation and may therefore release an electron to the conduction band before being lowered into the bandgap following lattice relaxation. If the excited complex resulting from either of the above processes contains an electron in a V_s state, R-Cu emission can subsequently occur. Otherwise, an electron must be recaptured by the complex into a V_s state for R-Cu emission to occur, leading to a longer emission lifetime. Based on this observation, the electron occupations of the defect levels in Figure 5b indicate how the charge state prior to excitation determines the possible emission pathways, which define the emission lifetime and the energy of the R-Cu PL.

R-Cu Emission Dynamics. Figure 6 shows how the spectral and temporal characteristics of the R-Cu PL as a function of temperature provide detailed insight regarding the emission mechanisms and the states involved. At temperatures from 19 to 290 K, we measure the PL emission spectrum to find the peak λ_{em}, and we then measure the corresponding PL decay curve for that λ_{em}. The PL spectra at each temperature are converted to energy units (see Methods) and fit using Gaussian functions to extract the peak energies (E_{em}) and integrated intensities. The emission spectra at 19, 110, 150, 190, and 290 K are plotted as examples in Figure 6a along with the corresponding fit results. The spectral data for all measurement temperatures are shown in the pseudocolor plot of the inset, and fitted spectra for all measurement temperatures not included in Figure 6a are shown in SI Section 8. For the PL decay measurements at each temperature (Figure 6b), we find that a triexponential decay model most effectively describes the data compared to fitting with one, two, or four exponential terms or a stretched exponential decay function. The best-fit lifetime components, τ_i for i = 1, 2, 3, at every temperature are plotted in Figure 6c, showing three, well-separated decay lifetimes.

At the lowest measurement temperature of 19 K (Figure 6d), we acquire PL decay curves across the R-Cu emission band with 2.5 nm resolution, and we fit the data using the triexponential model with fixed lifetimes based on the fit results from Figure 6c. Figure 6d shows the PL amplitudes corresponding to the decay components τ_1, τ_2, and τ_3 as a function of λ_{em}. The fast component τ_1 likely reflects the tail of one or more peaks outside the R-Cu emission band, with little spectral dependence. However, separating the slow (τ_3) and fast (τ_2) PL contributions this way reveals the presence of two distinct peaks at 1.73 and 1.82 eV. The observation of energetically distinct PL peaks with different lifetimes is consistent with the coexistence of two separate radiative transitions.

Figure 6e shows the integrated PL intensity over the R-Cu band and best-fit E_{em} at every temperature, extracted from Gaussian fits to the PL data in Figure 6a. As noted previously, E_{em} blueshifts as the temperature increases, and Figure 6e illustrates that the shift occurs nonlinearly, with a marked inflection between 100 and 200 K and saturation at both higher and lower temperatures. Meanwhile, the R-Cu emission intensity decreases with increasing temperature from 19 to 190 K, then plateaus between 190 and 210 K, before decreasing again at higher temperatures. The initial decrease in intensity is consistent with quenching through thermally activated non-radiative recombination pathways and is typical for defect emission. The plateau in the intensity between 190 and 210 K is anomalous and can be explained by a temporary increase in PL intensity from a subset of radiative states, referred to as negative thermal quenching (NTQ). NTQ is occasionally observed in defect emission, for example, in the case of the 2.65 eV PL (referred to as the YS1 peak) from ZnS:I,[32] and it has generally been explained by thermally activated carrier transfer from lower- to higher-energy emissive defect states. ZnS:Cu NCs have been synthesized in water at room temperature with the same $Cu(CH_3COO)_2$ precursor[9] and then subsequently annealed at 450 °C to intensify R-Cu PL, but the resulting red peak (600 nm at room temperature) is not resolvable from other emission peaks when the temper-

https://doi.org/10.1021/acsnano.3c00191
ACS Nano 2023, 17, 5963−5973

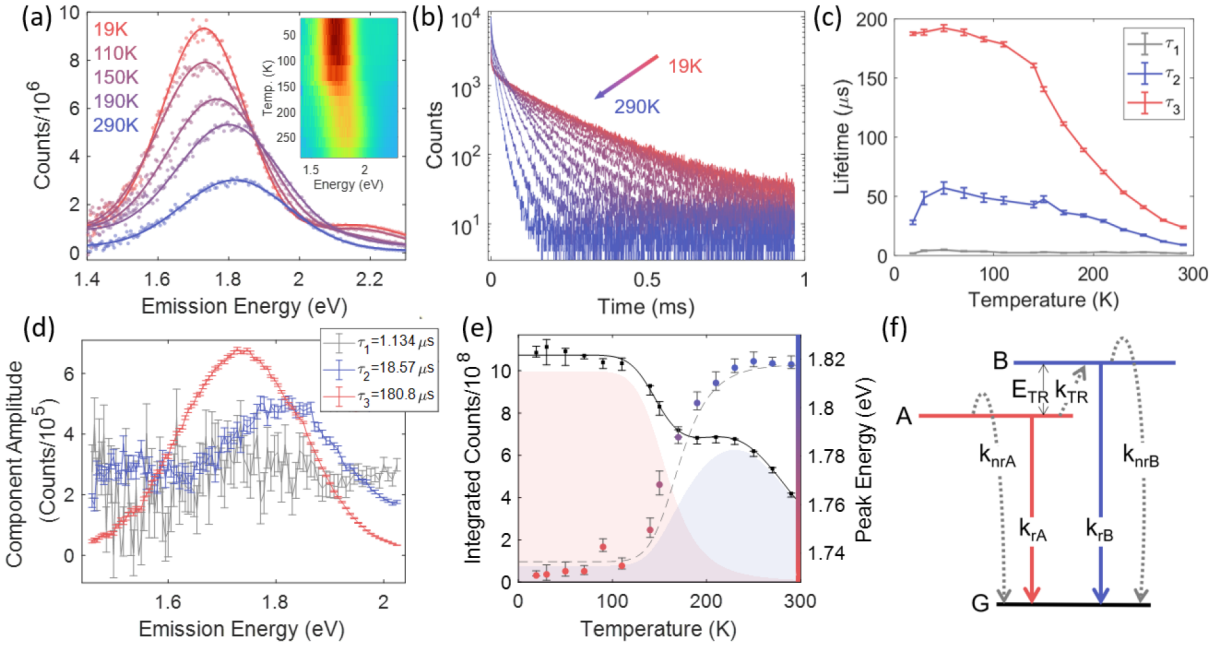

Figure 6. R-Cu emission dynamics. (a) PL spectra measured at temperatures ranging from 19 to 290 K (data points for five representative temperatures are shown, with all data plotted in the inset) and Gaussian fits (solid traces). (b) Time-dependent PL emission following pulsed excitation at λ_{ex} = 375 nm, measured at the peak PL wavelength for temperatures from 19 to 290 K. (c) PL decay lifetimes extracted from a triexponential fit to the time-dependent PL curves in (d) at each measurement temperature. (d) Amplitudes of each triexponential decay component at a single temperature (19 K) as a function of emission energy. (e) Integrated emission intensity (black points) and peak energy (colored points) as a function of temperature, extracted from the Gaussian fits of (a). Error bars represent 68% confidence intervals from fit results. The solid black curve is a fit to the intensity data using the model described in the text. Red and blue shaded regions represent the relative temperature-dependent intensities $I_A(T)$ and $I_B(T)$ from the best-fit model, and the dashed curve is a sum of the two emission energies resolved in (d), weighted by their corresponding best-fit emission intensities. (f) Energy level diagram showing two manifolds of states inside the ZnS bandgap with coupled relaxation processes, where radiative recombination from A to G results in 1.73 eV emission and radiative recombination from B to G results in 1.82 eV emission.

ature is less than 220 K, making it impossible to observe a similar NTQ or blueshift.

In Figure 6f, we propose an empirical model to capture both the temperature-dependent blueshift and the NTQ of R-Cu emission. Motivated by the time-resolved observations of Figure 6d, we include two radiative recombination transitions with emission energies at 1.73 eV (A → G) and 1.82 eV (B → G), corresponding to two distinct excited-state configurations. These radiative transitions compete with thermally activated, nonradiative transitions that generally tend to quench the emission at elevated temperatures. However, as carriers are thermally excited from state A to state B at temperatures with thermal energy corresponding to the energy offset E_{TR}, the faster B → G transition increasingly becomes the dominant radiative recombination pathway, resulting in blueshifted PL and temporary NTQ. This mechanism is consistent with our observation that inflection points in the PL intensity align with the onset and saturation of the blueshift in E_{em}.

To quantify this model, we derive the following analytical expressions for the temperature-dependent PL intensities, $I(A)$ and $I(B)$, from the radiative transitions occurring from excited states A and B, respectively:

$$I_A(T) = I_A(0)\frac{k_{rA}}{k_{rA} + k_{nrA} + k_{TR}} \quad (1)$$

$$I_B(T) = I_B(0)\frac{k_{rB}}{k_{rB} + k_{nrB}} + I_A(0)\frac{k_{TR}k_{rB}}{k_{rB} + k_{nrB}} \quad (2)$$

Here, k_{rA} and k_{rB} are the radiative recombination rates shown in Figure 6f (solid lines), which are independent of temperature. The terms k_{nrA} and k_{nrB} are rates for nonradiative relaxation, and k_{TR} is the rate for nonradiative transfer between states A and B (dashed lines in Figure 6f). These nonradiative rates are temperature-dependent with the form $k_j = \Gamma_j \exp(-E_j/k_BT)$, where Γ_j is a proportionality constant, E_j is the activation energy of the transition, and k_B is Boltzmann's constant. See SI Section 9 for a derivation of these expressions.

The sum of eqs 1 and 2 gives the total PL intensity as a function of temperature. This expression is used as a model to fit the temperature-dependent PL intensity data in Figure 6e, from which we extract best-fit values for the energies E_{nrA}, E_{nrB}, and E_{TR}. The best-fit value of E_{TR} is 153 ± 22 meV. Details of the fitting procedure along with best-fit results for other parameters are included in SI Section 9. It is worth mentioning that our expression for the temperature-dependent PL intensity resembles an Arrhenius equation with an NTQ term, as in the case of ZnS:I,[33] and we have concluded that it is not possible to obtain an intensity curve with the measured temperature dependence by considering an Arrhenius equation with only positive thermal quenching terms. To confirm the validity of this model, the dashed curve in Figure 6e represents a weighted sum of the 1.73 and 1.82 eV PL contributions, with weights determined by the best-fit $I_A(T)$ and $I_B(T)$ values (the intensities are represented by shaded regions in Figure 6e). We recover a temperature-dependent emission energy that closely tracks the measured ~90 meV blueshift of E_{em} between 19 and 290 K.

https://doi.org/10.1021/acsnano.3c00191
ACS Nano 2023, 17, 5963−5973

The states A and B in our empirical model might be associated with different charge states or spatial configurations of Cu_{Zn} and V_S. Based on the defect level calculations in Figure 5b, the energy levels associated with both Cu_{Zn} and V_S shift in different charge states, as do the degree of orbital hybridization between Cu_{Zn} and V_S states. The emission energies and lifetimes associated with different charge states should therefore be different. (Note, however, that this remains a qualitative observation since the ground-state PDOS calculations do not fully capture the energies of excited-state configurations, which would be required to calculate emission energies.) We also consider the possibility that defects outside of Cu_{Zn}-V_S complexes are responsible for activating R-Cu at low or high temperatures. Possible candidates for defects creating donor levels in ZnS include Zn_i or Cu_i interstitial defects, as well as lone V_S defects. Cu_i is a shallow donor in ZnS[34] and is therefore unlikely to play a role as the donor level in R-Cu emission at any temperature. At low temperatures, it is possible that the primary donors in the R-Cu emission mechanism are lone V_S defects in the NC core or at the surface, because their more distant interaction with Cu_{Zn} relative to V_S in a Cu_{Zn}-V_S complex would be consistent with longer-lived and lower-energy radiative recombination. The inverse situation, in which lone Cu_{Zn} defects are primary acceptors at low temperatures, would be similar in a model considering holes instead of electrons; however, this situation is less likely given the high concentration of V_S defects expected to exist at the NC surface compared to the Cu_{Zn} defects in these samples. Ultimately, carrier transfer between two manifolds of states may be advantageous for potential defect qubit architectures if it is found to be spin-dependent, or mitigated if it is found to be detrimental.[35]

We also considered other potential explanations for the R-Cu blueshift and NTQ. Previous reports of blueshifted R-Cu emission upon increasing temperature from bulk ZnS:Cu were attributed to changing occupation in the vibrational levels of a highly localized center.[18] However, that explanation is not consistent with the saturation in the blueshift at high temperatures, which we clearly observe and which also appears to occur in their measurement around 200 K. Characteristic defect PL in bulk and nanocrystalline ZnS:Mn also exhibits a blueshift upon increasing temperature with magnitudes between 25 and 80 meV, which has been attributed to crystal field variations due to lattice expansion.[36,37] The crystal field explanation would also not predict saturating behavior, and accordingly the temperature-dependent blueshift of ZnS:Mn defect PL does not saturate, in contrast to the R-Cu observations. As an additional indication that crystal field effects cannot sufficiently explain the measured R-Cu blueshift, we calculate only a 16 ± 0.01 meV increase in the energy separation between Cu_{Zn} and V_S levels of the neutral complex upon performing DFT computations with different ZnS lattice constants, corresponding to 0 and 300 K based on the ZnS thermal expansion coefficient.[38] It is worth noting that in nanocrystalline ZnS:Mn, NTQ has also been reported between 50 and 300 K, with positive thermal quenching resuming above 300 K.[37] The authors attributed the NTQ to the thermal depopulation of localized trap states created by lattice defects, organic impurities, and surface defects, which are all expected to be more prevalent in NCs compared to bulk materials. None of the above alternative models for the R-Cu blueshift and NTQ can explain the clear presence of two distinct emission peaks with different radiative lifetimes at low temperature, as we observe in Figure 6d, nor do they capture the correspondence in Figure 6e between the NTQ regime and the blueshift occurring at approximately the same temperature.

CONCLUSION

We present a synthetic method for obtaining colloidal ZnS:Cu NCs that emit primarily R-Cu, with a tailorable intensity depending on the Cu concentration. Using time- and temperature-resolved measurements and first-principles calculations, we find the sub-bandgap PL is consistent with radiative transitions from two, coupled manifolds of states involving Cu_{Zn}-V_S complexes. In the future, experimental methods enabled by colloidal NC platforms will clarify the importance of defect type, location, concentration, and charge state on R-Cu PL. For example, postsynthesis NC modification (e.g., surface treatments that passivate traps and for remote doping, cation exchange, or sulfidation) and the growth of core−shell heterostructures will controllably alter the environments and compositions of defects as well as the Fermi level of NCs. Spectroelectrochemical measurements of colloidal NC dispersions can also reveal the relationship between defect PL and the NC Fermi level. These studies, combined with ESR and ODMR measurements that probe spin transitions, will yield valuable information about the R-Cu electronic structure and spin-dependent optical properties for potential development of R-Cu centers as defect qubits.

Colloidal NC hosts will also facilitate the isolation and study of individual R-Cu color centers, compared to bulk hosts, which have typically been used for the development of color centers as defect qubits. The deposition of sparse dispersions of colloidal NCs reduces the bulk purity requirement for single-quantum-emitter measurements by thousands of times.[5,39] Furthermore, established methods for colloidal NC luminescence enhancement by integration with resonant photonic cavities or plasmonic nanostructures can improve the efficiency of quantum emitter measurements by reducing PL lifetimes through Purcell enhancement.[40,41]

Our investigation of R-Cu color centers also motivates studying other transition-metal-vacancy complexes in ZnS as potential defect qubits; for example, transition metals with fewer d-shell electrons than Cu, when placed in a similar defect and charge configuration, could produce a higher ground-state spin and a greater number of internal radiative transitions. Such theoretically interesting materials systems are readily available for experimentation through colloidal NC synthesis methods, which are fast and accessible compared to methods that exist for bulk crystals and can be atomically precise.[42] All of the above opportunities will facilitate the development of color centers in ZnS as quantum defects while generally motivating colloidal NCs as a host for quantum defect development and engineering.

METHODS

Synthesis of Colloidal ZnS:Cu NCs. A 10 mL solution of $Cu(CH_3COO)_2{\cdot}H_2O$ in DI water is prepared with the appropriate molar concentration of Cu, i.e., 0.05%, 0.075%, or 0.1% of the molar concentration of Zn in the reaction. Then 0.1 mL of this solution is added to a 50 mL three-necked flask containing 20 mmol of OM. The mixture is degassed for 45 min at 120 °C before the injection of 20 mmol of OA and 0.2 mmol of $Zn(Ddtc)_2$, followed by 45 min additional degassing. The vessel is then heated to 300 °C under a nitrogen atmosphere and maintained at 300 °C for 45 min. It is then left to cool to 60 °C. The cooled contents are mixed with excess

https://doi.org/10.1021/acsnano.3c00191
ACS Nano 2023, 17, 5963−5973

ethanol, and NCs are collected via centrifugation, washed in ethanol, and redispersed in hexanes to a concentration of 10 mg/mL.

Tools and Instrumentation. ICP-OES measurements are collected using a SPECTRO GENESIS ICP-OES spectrometer. To collect TEM images, 2 mg/mL NC dispersions in hexanes are drop-cast onto carbon-coated copper grids and imaged using a JEOL-1400 TEM. TEM images are analyzed using Fiji.[43] Absorption spectra are measured using an Agilent Cary 5000 spectrometer. PL and PLE spectra are measured using an Edinburgh Instruments FLS1000 spectrometer with a PMT-980 photodetector. For continuous PL and PLE measurements, the excitation source is a 450 W Xe lamp. For time-resolved measurements, the excitation source is a 375 nm Picoquant LDH-series laser diode. For temperature-controlled measurements, samples are placed in an evacuated Advanced Research Systems DE-202 cryostat. The illustration of a spherical ZnS NC in the Table of Contents graphic was generated using NanoCrystal.[44]

Analysis of PL Emission Spectra. PL spectra are measured as a distribution function of wavelength and converted to energy units prior to Gaussian fitting to extract the positions and widths of individual peaks. To properly account for the nonlinear relationship between wavelength and energy, we scale the spectra using the appropriate Jacobian transformation:[45]

$$f(E) = f(\lambda)\frac{hc}{E^2} \tag{3}$$

The broad spectral range and large peak widths in our measurements make this scaling factor critical in our analysis. We find that simply converting the peak wavelengths in the as-measured spectra to energy units would result in the extraction of dramatically incorrect peak energies. This can be seen in the results of Table 1, which take the scaling factor into account prior to peak extraction on an energy scale.

Computational Details. The electronic structures of the bulk ZnS and defect centers such as Cu_{Zn} and Cu_{Zn}-V_S complexes in ZnS are studied using DFT with the Vienna Simulation Package[46] (VASP). VASP employs the Perdew–Burke–Ernzerhof (PBE) functional for the exchange and correlation within the augmented plane wave (PAW) scheme.[47,48] For the supercell, we use two different sizes: one with 64 atoms and the other with 212 atoms. Both calculations yield the same results for formation energies, electronic band structure, and total and projected DOS. We use a total energy cutoff of 300 eV and 6 × 6 × 6 and 12 × 12 × 12 Monkhorst–Pack *k*-point meshes for the density of states calculations in the larger and smaller supercells, respectively.

The formation energies of differently charged configurations are calculated from the well-known defect formula[49]

$$E_f^q(\varepsilon_F) = E_{tot}^q - E_{tot}^{bulk} + E_{corr} + \sum_i n_i\mu_i + q(E_{VBM} + \varepsilon_F + \Delta_{q/b}) \tag{4}$$

where the first two terms are the total energies of the bulk and defected supercell, and the correction term E_{corr} (first-order Makov–Payne correction) originates from the interaction between periodic charged supercells. The chemical potentials μ_i correspond to adding Cu or removing Zn and S, ϵ_F is the Fermi level, and E_{VBM} is the valence band maximum. The final term $\Delta_{q/b}$ is the potential alignment between the valence band edges for the bulk and neutral or charged supercells.

Hybrid DFT calculations are also completed for the 64-atom supercell using the B3LYP hybrid functional. Charge transition levels of the formation energies are not affected by the hybrid calculation, but the conduction band minimum is pushed from about 2.14 to 3.55 eV, yielding a bandgap energy closer to that which is observed experimentally (SI Section 10).

ASSOCIATED CONTENT

Supporting Information

The Supporting Information is available free of charge at https://pubs.acs.org/doi/10.1021/acsnano.3c00191.

Additional data and analysis concerning nonnegative matrix factorization of PL spectral components, NC bandgap energies, surface treatments, R-Cu PL lifetime, temperature-dependent PL/PLE maps, and Gaussian fitting of PL spectra, along with derivations of analytical eqs 1 and 2 and hybrid DFT calculations (PDF)

AUTHOR INFORMATION

Corresponding Authors

Lee C. Bassett − *Department of Electrical and Systems Engineering, University of Pennsylvania, Philadelphia, Pennsylvania 19104, United States;* orcid.org/0000-0001-8729-1530; Email: lbassett@seas.upenn.edu

Cherie R. Kagan − *Department of Electrical and Systems Engineering and Department of Chemistry, University of Pennsylvania, Philadelphia, Pennsylvania 19104, United States; Department of Materials Science and Engineering and Department of Materials Science and Engineering, University of Pennsylvania, Philadelphia, Pennsylvania 19104, United States;* orcid.org/0000-0001-6540-2009; Email: kagan@seas.upenn.edu

Authors

Sarah M. Thompson − *Department of Electrical and Systems Engineering, University of Pennsylvania, Philadelphia, Pennsylvania 19104, United States;* orcid.org/0000-0002-1870-0633

Cüneyt Şahin − *UNAM − National Nanotechnology Research Center and Institute of Materials Science and Nanotechnology, Bilkent University, Ankara, TR 06800, Turkey; Department of Physics and Astronomy, University of Iowa, Iowa City, Iowa 52242, United States*

Shengsong Yang − *Department of Chemistry, University of Pennsylvania, Philadelphia, Pennsylvania 19104, United States;* orcid.org/0000-0002-1386-7549

Michael E. Flatté − *Department of Physics and Astronomy, University of Iowa, Iowa City, Iowa 52242, United States; Department of Applied Physics, Eindhoven University of Technology, 5600 MB Eindhoven, The Netherlands;* orcid.org/0000-0001-5093-1549

Christopher B. Murray − *Department of Chemistry, University of Pennsylvania, Philadelphia, Pennsylvania 19104, United States*

Complete contact information is available at: https://pubs.acs.org/10.1021/acsnano.3c00191

Notes

The authors declare no competing financial interest.

ACKNOWLEDGMENTS

This work was supported by the National Science Foundation under award DMR-2019444 (S.Y., C.B.M., L.C.B., and C.R.K., for synthesis, measurements, and analysis) and DMREF awards DMR-1922278 (L.C.B.) and DMR-1921877 (C.S. and M.E.F.) for theory, first-principles calculations, and data analysis. S.M.T. acknowledges support from the National Science Foundation Graduate Research Fellowship under Grant No. DGE-1845298.

REFERENCES

(1) Castelletto, S.; Boretti, A. Color Centers in Wide-Bandgap Semiconductors for Subdiffraction Imaging: A Review. *Advanced Photonics* **2021**, *3*, 1−20.

(2) Lahariya, V.; Dhoble, S. J. Development and Advancement of Undoped and Doped Zinc Sulfide for Phosphor Application. *Displays* **2022**, *74*, 102186.

(3) Norman, V. A.; Majety, S.; Wang, Z.; Casey, W. H.; Curro, N.; Radulaski, M. Novel Color Center Platforms Enabling Fundamental Scientific Discovery. *InfoMat* **2021**, *3*, 869−890.

(4) Bassett, L. C.; Alkauskas, A.; Exarhos, A. L.; Fu, K.-M. C. Quantum Defects by Design. *Nanophotonics* **2019**, *8*, 1867−1888.

(5) Kagan, C. R.; Bassett, L. C.; Murray, C. B.; Thompson, S. M. Colloidal Quantum Dots as Platforms for Quantum Information Science. *Chem. Rev.* **2021**, *121*, 3186−3233.

(6) Stewart, C.; Kianinia, M.; Previdi, R.; Tran, T. T.; Aharonovich, I.; Bradac, C. Quantum Emission from Localized Defects in Zinc Sulfide. *Opt. Lett.* **2019**, *44*, 4873.

(7) Hoang, K. Rare-Earth Defects and Defect-Related Luminescence in ZnS. *J. Appl. Phys.* **2022**, *131*, 015705.

(8) Knowles, K. E.; Hartstein, K. H.; Kilburn, T. B.; Marchioro, A.; Nelson, H. D.; Whitham, P. J.; Gamelin, D. R. Luminescent Colloidal Semiconductor Nanocrystals Containing Copper: Synthesis, Photophysics, and Applications. *Chem. Rev.* **2016**, *116*, 10820−10851.

(9) Bol, A. A.; Ferwerda, J.; Bergwerff, J. A.; Meijerink, A. Luminescence of Nanocrystalline ZnS:Cu2+. *J. Lumin.* **2002**, *99*, 325−334.

(10) Curcio, A. L.; da Silva, L. F.; Bernardi, M. I. B.; Longo, E.; Mesquita, A. Nanostructured ZnS:Cu phosphor: Correlation Between Photoluminescence Properties and Local Structure. *J. Lumin.* **2019**, *206*, 292−297.

(11) Shionoya, S.; Urabe, K.; Koda, T.; Era, K.; Fujiwara, H. Nature of the Red-Copper Luminescence Centre in ZnS Crystals as Elucidated by Plolarization Measurements. *J. Phys. Chem. Solids* **1966**, *27*, 865−869.

(12) Yen, W. M. W. M.; Shionoya, S.; Yamamoto, H. *Phosphor Handbook*; CRC Press/Taylor and Francis, 2007; p 1051.

(13) Doherty, M. W.; Manson, N. B.; Delaney, P.; Hollenberg, L. C. L. The Negatively Charged Nitrogen-Vacancy Centre in Diamond: The Electronic Solution. *New J. Phys.* **2011**, *13*, 025019.

(14) Koehl, W. F.; Buckley, B. B.; Heremans, F. J.; Calusine, G.; Awschalom, D. D. Room Temperature Coherent Control of Defect Spin Qubits in Silicon Carbide. *Nature* **2011**, *479*, 84−87.

(15) Holton, W. C.; De Wit, M.; Watts, R. K.; Estle, T. L.; Schneider, J. Paramagnetic Copper Centers in ZnS. *J. Phys. Chem. Solids* **1969**, *30*, 963−977.

(16) Wolfowicz, G.; Heremans, F. J.; Anderson, C. P.; Kanai, S.; Seo, H.; Gali, A.; Galli, G.; Awschalom, D. D. Quantum Guidelines for Solid-State Spin Defects. *Nature Reviews Materials* **2021**, *6*, 906−935.

(17) Zhang, Y.; Xu, H.; Wang, Q. Ultrathin Single Crystal ZnS Nanowires. *Chem. Commun.* **2010**, *46*, 8941−8943.

(18) Shionoya, S.; Koda, T.; Era, K.; Fujiwara, H. Nature of the Luminescence Transitions in ZnS Crystals. *J. Phys. Soc. Jpn.* **1964**, *19*, 1157.

(19) Denzler, D.; Olschewski, M.; Sattler, K. Luminescence Studies of Localized Gap States in Colloidal ZnS Nanocrystals. *J. Appl. Phys.* **1998**, *84*, 2841.

(20) Goswami, N.; Sen, P. Photoluminescent Properties of ZnS Nanoparticles Prepared by Electro-Explosion of Zn Wires. *J. Nanopart. Res.* **2007**, *9*, 513−517.

(21) Ramasamy, V.; Praba, K.; Murugadoss, G. Synthesis and Study of Optical Properties of Transition Metals Doped ZnS Nanoparticles. *Spectrochimica Acta Part A: Molecular and Biomolecular Spectroscopy* **2012**, *96*, 963−971.

(22) Saleh, M.; Lynn, K. G.; Jacobsohn, L. G.; McCloy, J. S. Luminescence of Undoped Commercial ZnS Crystals: A Critical Review and New Evidence on the Role of Impurities Using Photoluminescence and Electrical Transient Spectroscopy. *J. Appl. Phys.* **2019**, *125*, 075702.

(23) Car, B.; Medling, S.; Corrado, C.; Zhang, J. Z. Nanoscale Probing the Local Structure of Dilute Cu Dopants in Fluorescent ZnS Nanocrystals Using EXAFS. *Nanoscale* **2011**, *3*, 4182−4189.

(24) Erwin, S. C.; Zu, L.; Haftel, M. I.; Efros, A. L.; Kennedy, T. A.; Norris, D. J. Doping Semiconductor Nanocrystals. *Nature* **2005**, *436*, 91−94.

(25) Goodwin, E. D.; Diroll, B. T.; Oh, S. J.; Paik, T.; Murray, C. B.; Kagan, C. R. Effects of Post-Synthesis Processing on CdSe Nanocrystals and Their Solids: Correlation between Surface Chemistry and Optoelectronic Properties. *J. Phys. Chem. C* **2014**, *118*, 27097−27105.

(26) Oh, S. J. S.; Berry, N. E. N.; Choi, J.-H.; Gaulding, E. A.; Lin, H.; Paik, T.; Diroll, B. B. T.; Muramoto, S.; Murray, C. B. C.; Kagan, C. C. R. Designing High-Performance PbS and PbSe Nanocrystal Electronic Devices Through Stepwise, Post-Synthesis, Colloidal Atomic Layer Deposition. *Nano Lett.* **2014**, *14*, 1559−1566.

(27) Kim, D. K.; Fafarman, A. T.; Diroll, B. T.; Chan, S. H.; Gordon, T. R.; Murray, C. B.; Kagan, C. R. Solution-Based Stoichiometric Control over Charge Transport in Nanocrystalline CdSe Devices. *ACS Nano* **2013**, *7*, 8760−70.

(28) Kripal, R.; Gupta, A. K.; Mishra, S. K.; Srivastava, R. K.; Pandey, A. C.; Prakash, S. G. Photoluminescence and Photoconductivity of ZnS:Mn2+ Nanoparticles Synthesized via Co-Precipitation Method. *Spectrochimica Acta Part A: Molecular and Biomolecular Spectroscopy* **2010**, *76*, 523−530.

(29) Peka, P.; Schulz, H.-J. Empirical One-Electron Model of Optical Transitions in Cu-doped ZnS and CdS. *Physica B* **1994**, *193*, 57−65.

(30) Chu, X.-Y.; Wang, X.-N.; Li, J.-H.; Yao, D.; Fang, X.; Fang, F.; Wei, Z.-P.; Wang, X.-H. Influence Factors and Mechanism of Emission of ZnS:Cu Nanocrystals. *Chinese Physics B* **2015**, *24*, 067805.

(31) Koda, T.; Shionoya, S. Nature of the Self-Activated Blue Luminescence Center in Cubic ZnS:Cl Single Crystals. *Phys. Rev.* **1964**, *136*, A541−A555.

(32) Yokogawa, T.; Taguchi, T.; Fujita, S.; Sato, M. Intense Blue-Emission Band and the Fabrication of Blue Light Emitting Diodes in I-Doped and Ag-Ion-Implanted Cubic ZnS. *IEEE Trans. Electron Devices* **1983**, *30*, 30.

(33) Shibata, H. Negative Thermal Quenching Curves in Photoluminescence of Solids. *Denshi Gijutsu Sogo Kenkyusho Iho/Bulletin of the Electrotechnical Laboratory* **1998**, *62*, 35−41.

(34) Hoang, K.; Latouche, C.; Jobic, S. Defect Energy Levels and Persistent Luminescence in Cu-doped ZnS. *Comput. Mater. Sci.* **2019**, *163*, 63−67.

(35) Hopper, D.; Shulevitz, H.; Bassett, L. Spin Readout Techniques of the Nitrogen-Vacancy Center in Diamond. *Micromachines* **2018**, *9*, 437.

(36) Chen, W.; Su, F.; Li, G.; Joly, A. G.; Malm, J. O.; Bovin, J. O. Temperature and Pressure Dependences of the Mn2+ and Donor-Acceptor Emissions in ZnS:Mn2+ Nanoparticles. *J. Appl. Phys.* **2002**, *92*, 1950−1955.

(37) Park, J. S.; Mho, S. W.; Choi, J. C. Abnormal Thermal Properties of ZnS:Mn2+ Nanophosphor. *Journal of the Korean Physical Society* **2007**, *50*, 571−574.

(38) Wang, S. Q. First-Principles Study of the Anisotropic Thermal Expansion of Wurtzite ZnS. *Appl. Phys. Lett.* **2006**, *88*, 061902.

(39) Shulevitz, H. J.; Huang, T.-y.; Xu, J.; Neuhaus, S. J.; Patel, R. N.; Choi, Y. C.; Bassett, L. C.; Kagan, C. R. Template-Assisted Self-Assembly of Fluorescent Nanodiamonds for Scalable Quantum Technologies. *ACS Nano* **2022**, *16*, 1847−1856.

(40) Saboktakin, M.; Ye, X.; Chettiar, U.; Engheta, N.; Murray, C.; Kagan, C. Plasmonic Enhancement of Nanophosphor Upconversion Luminescence in Au Nanohole Arrays. *ACS Nano* **2013**, *7*, 7186.

(41) Raha, M.; Chen, S.; Phenicie, C. M.; Ourari, S.; Dibos, A. M.; Thompson, J. D. Optical Quantum Nondemolition Measurement of a Single Rare Earth Ion Qubit. *Nat. Commun.* **2020**, *11*, 1605.

https://doi.org/10.1021/acsnano.3c00191
ACS Nano 2023, 17, 5963−5973

(42) Muckel, F.; Yang, J.; Lorenz, S.; Baek, W.; Chang, H.; Hyeon, T.; Bacher, G.; Fainblat, R. Digital Doping in Magic-Sized CdSe Clusters. *ACS Nano* **2016**, *10*, 7135−7141.
(43) Schindelin, J.; Arganda-carreras, I.; Frise, E.; Kaynig, V.; Longair, M.; Pietzsch, T.; Preibisch, S.; Rueden, C.; Saalfeld, S.; Schmid, B.; et al. Fiji: An Open-Source Platform for Biological-Image Analysis. *Nat. Methods* **2019**, *9*, 676−682.
(44) Chatzigoulas, A.; Karathanou, K.; Dellis, D.; Cournia, Z. NanoCrystal: A Web-Based Crystallographic Tool for the Construction of Nanoparticles Based on Their Crystal Habit. *J. Chem. Inf. Model.* **2018**, *58*, 2380−2386.
(45) Mooney, J.; Kambhampati, P. Get the Basics Right: Jacobian Conversion of Wavelength and Energy Scales for Quantitative Analysis of Emission Spectra. *J. Phys. Chem. Lett.* **2013**, *4*, 3316−3318.
(46) Kresse, G.; Furthmüller, J. Efficient Iterative Schemes for Ab Initio Total-Energy Calculations Using a Plane-Wave Basis Set. *Phys. Rev. B* **1996**, *54*, 11169−11186.
(47) Kresse, G.; Furthmüller, J. Efficiency of Ab-Initio Total Energy Calculations for Metals and Semiconductors Using a Plane-Wave Basis Set. *Comput. Mater. Sci.* **1996**, *6*, 15−50.
(48) Kresse, G.; Joubert, D. From Ultrasoft Pseudopotentials to the Projector Augmented-Wave Method. *Phys. Rev. B* **1999**, *59*, 1758−1775.
(49) Zhang, S. B.; Northrup, J. E. Chemical Potential Dependence of Defect Formation Energies in GaAs: Application to Ga Self-Diffusion. *Phys. Rev. Lett.* **1991**, *67*, 2339−2342.

https://doi.org/10.1021/acsnano.3c00191
ACS Nano 2023, 17, 5963−5973